Microstructures Of Irradiated And Mechanically Deformed Metals And Alloys: Fundamental Aspects

S.J. Zinkle, N. Hashimoto, Y. Matsukawa, R.E. Stoller and Yu.N. Osetsky
Metals and Ceramics Division, Oak Ridge National Laboratory, P.O. Box 2008, Oak Ridge, TN 37831-6138 USA

ABSTRACT

Recent molecular dynamics and transmission electron microscopy results on irradiated metallic materials are reviewed, with an emphasis on defect production in the displacement cascade and the fluence- and temperature-dependent accumulation of defect clusters. Materials analyzed include Fe, V, Cu, austenitic stainless steel, V4%Cr4%Ti, and ferritic/martensitic steel. Intrinsic differences between the defect accumulation behavior of body centered cubic (BCC) and face centered cubic (FCC) metals are highlighted. Results on the temperature-dependent vacancy cluster density of Cu are discussed in terms of thermal stability of stacking fault tetrahedra (SFTs). Finally, recent results on deformation behavior of irradiated, quenched, and deformed metals are discussed, with particular emphasis on flow localization mechanisms (e.g., dislocation channeling), and experimental and molecular dynamics studies of the detailed dislocation-defect cluster interactions.

INTRODUCTION

Pronounced microstructural changes are induced in pure metals and alloys by energetic particle irradiation. These microstructural changes can result in large changes in the mechanical and physical properties of materials. Fundamental theoretical and experimental investigations of these microstructural changes are indispensable for understanding the underlying physical processes that drive the microstructural changes. In the following, a brief review is presented on a few of the key microstructural changes that occur in irradiated metals and alloys, with an emphasis on results obtained from molecular dynamics (MD) simulations and transmission electron microscope (TEM) studies. The first section of this review concentrates on defect cluster accumulation. Recent results on interactions between moving dislocations and defect clusters (including the formation of cleared dislocation channels) are summarized in the latter section of this report.

DEFECT PRODUCTION

The intense atomic agitation that occurs during time scales of ~0.1 to 10 ps in energetic displacement cascades causes considerable recombination of the point defects that were originally produced by the primary knock on atom (PKA). Experimental studies and molecular dynamics simulations of energetic displacement cascades (PKA energies above ~10 keV) indicate that the ratio of initially displaced atoms to surviving displacements (at cryogenic temperatures, where long range point defect migration does not occur) is ~100 [1]. The recombination that occurs during the cooling phase of the displacement cascade causes the total number of surviving defects to become less than the value calculated according to the internationally accepted Norgett-Robinson-Torrens (NRT) model [2] for displacement damage [1,3,4]. Figure 1 summarizes the effect of PKA energy on the surviving defect fraction (normalized to the NRT displacement value), as calculated for Fe and Cu using MD simulations. The surviving defect fraction in Fe drops rapidly with increasing PKA energy up to ~10 keV (corresponding to the average cascade energy for fission reactor neutrons), and then remains nearly constant up to energies that exceed the average cascade energy for deuterium-tritium fusion reactor blanket conditions. The physical mechanism responsible for the decrease in surviving defect efficiency at energies up to 10 keV is associated with enhanced point defect recombination within the displacement cascade. At energies above ~10 keV in Fe, the
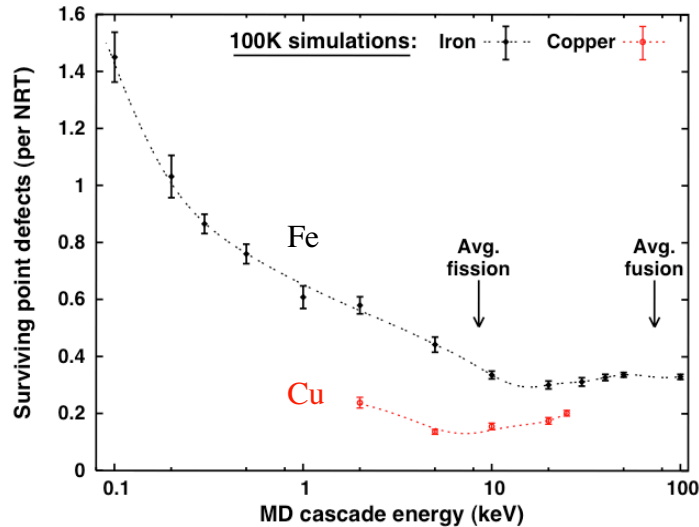
Figure 1. Surviving defect efficiency in Fe and Cu as a function of primary knock on atom energy, as calculated by molecular dynamics [5,6].

displacement cascade tends to split into multiple subcascades each with a maximum size comparable to that of a 10 keV cascade, which leads to a nearly constant surviving defect fraction of ~30% compared to the NRT displacement value [5,7-9]. Qualitatively similar behavior has been observed in numerous other FCC and BCC metals, although details such as the critical energy for subcascade formation and the high-energy asymptotic value of the surviving defect fraction depend on several material parameters including atomic mass and crystal structure [1,5,7,10]. As shown in Fig. 1, the calculated surviving defect fraction for Cu is generally less than that for Fe.

The detailed geometries of defect clusters formed directly within displacement cascades have been the subject of ongoing research. Early MD simulations reported formation of vacancy clusters of unspecified geometry (or occasionally faulted vacancy dislocation loops) and small interstitial planar clusters or collapsed interstitial loops [11-14]. Direct formation of stacking fault tetrahedra (SFTs) within individual displacement cascades has been recently observed during MD simulations of Cu [10,15-17]. Nearly perfect SFTs were observed to form within ~50 ps. An example of a nearly perfect SFT formed after ~20 ps in Cu with an edge length of ~2.4 nm (comparable to the experimentally observed size in neutron irradiated Cu [18]) is shown in Fig. 2. As shown in Fig. 3, the vacancy-rich core of the displacement cascade often collapses to truncated or overlapping SFTs in the MD simulations. Isolated point defects are distributed throughout the cascade and planar clusters of interstitial-type defects are formed near the periphery of the displacement cascade (Fig. 3). These planar clusters are either sessile faulted loops (upper right cluster in Fig. 3) or uncollapsed clusters (Fig. 3 bottom) calculated to be highly glissile which diffuse predominantly in one dimension along <110> directions on {111} close packed planes [10,19]. One-dimensional glissile interstitial clusters have also been observed in MD simulations of irradiated Fe [14,19].

Figure 4 compares the dose dependence of visible defect cluster density measured by TEM in neutron-irradiated copper and nickel for irradiation temperatures near room temperature [18,20]. These irradiation temperatures are below the temperature where vacancy-type defect clusters become thermally unstable in Cu and nickel, also known as the electrical resistivity Stage V recovery temperature [1]. For both materials, the defect cluster accumulation is initially linear with dose and approaches a constant density at high doses. The saturation high-dose density is associated with displacement cascades destroying pre-existing defect clusters ("cascade overlap" regime) [1,21]. The visible defect cluster density in Cu at low doses is approximately one order of magnitude higher than for Ni. There are insufficient Ni data at higher doses (>0.1 dpa) to determine whether the higher cluster density in Cu vs. Ni is maintained in the cascade overlap dose regime. The higher defect cluster production efficiency for Cu has been attributed to thermal spike effects associated with differences in electron-phonon coupling and melting temperature [22-24].
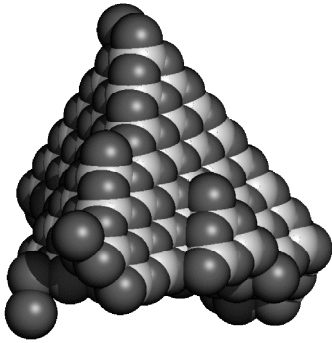
Figure 2. Example of a nearly perfect SFT produced in a 25 keV MD displacement cascade in Cu at 100 K [17].
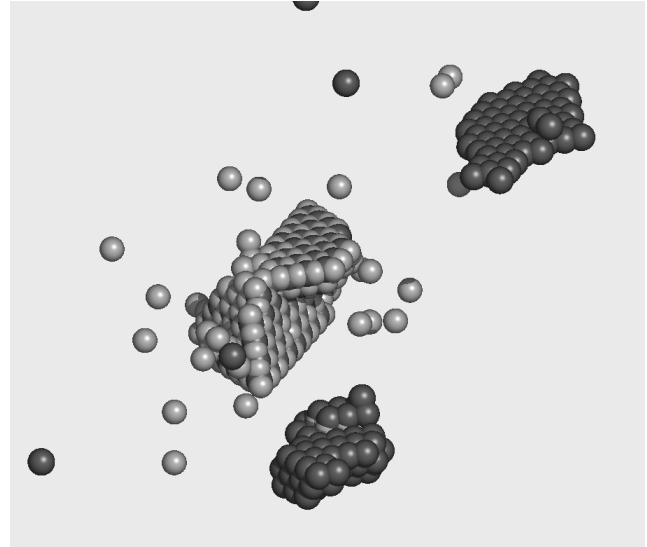

Figure 3. Defect cluster configurations produced in a 25 keV displacement cascade in Cu at 100 K. The dark gray circles denote interstitial atoms, and the light gray circles denote vacancies.

Defect clusters are visible in Cu and Ni at all irradiation doses. The presence of visible clusters even at very low doses near ~10^{-5} dpa (where the probability of cluster formation from point defect nucleation and growth processes is very small), along with the observed linear accumulation rate of defect cluster density versus dose, implies that defect clusters in irradiated Cu and Ni are produced directly in the displacement cascade. Figure 5 summarizes TEM measurements of the average defect cluster size in neutron and ion irradiated Cu for irradiation temperatures near room temperature. The measured defect cluster size in copper is nearly independent of dose over a wide range of dose levels [20,25-30]. The size independence illustrated in Fig. 5, along with recent MD simulation results (e.g., Figs. 2, 3), provides further evidence that visible defect clusters are directly
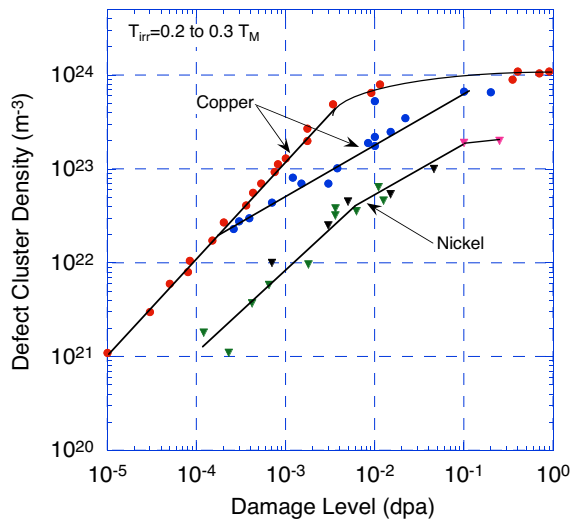

Figure 4. Dose dependence of visible defect cluster density in neutron irradiated Cu and Ni for irradiation near room temperature.
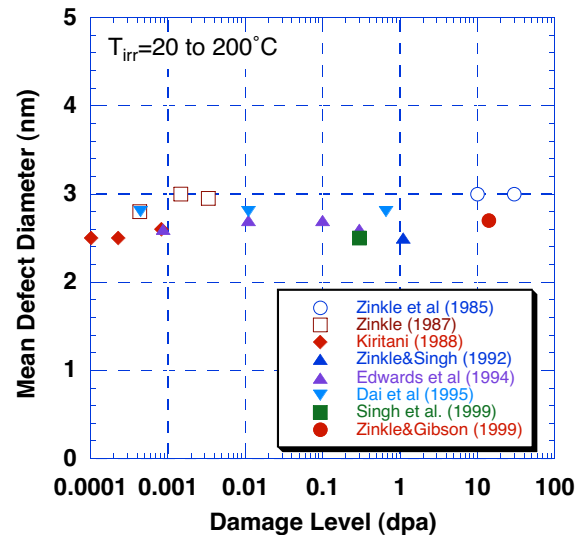

Figure 5. Summary of visible defect cluster size in neutron and ion irradiated Cu irradiated near room temperature.

formed in displacement cascades in Cu. It is worth noting that the defect cluster geometry in ion or neutron irradiated Cu near room temperature predominantly consists of vacancy-type SFTs over a wide range of doses [20,25-30]. On the other hand, the defect cluster geometry in Ni irradiated near room temperature initially consists predominantly of SFTs at low doses (<0.01 dpa) and evolves to predominantly interstitial-type dislocation loops at higher doses [20]. The fundamental physical mechanism responsible for this dramatically different defect cluster morphology evolution in two FCC metals that are neighbors in the periodic table has not yet been firmly determined.

Several TEM and electrical resistivity studies performed on irradiated Cu have reported an intermediate dose regime where the defect cluster density is proportional to the square root of dose [18,25,31-33]. The defect accumulation behavior was found to be linear at very low doses (<0.0001 dpa, where the probability of uncorrelated point defect recombination is negligible), and proportional to the square root of dose at higher doses (Fig. 4). The critical dose for transition from linear to square root behavior depends on the Cu purity, and may be associated with impurity trapping of freely migrating interstitial-type defects. Additional systematic work is needed to verify the presence and to understand the physical mechanisms responsible for this square root dose-dependent defect accumulation regime in copper and other pure metals.

Figure 6 compares the defect cluster accumulation behavior of neutron irradiated copper and iron for irradiation near room temperature to damage levels of 0.0001 to 1 dpa. Defect clusters are visible in copper at all irradiation doses, and as mentioned previously, appear to be directly formed in displacement cascades with an average size near ~2 nm. The visible defect clusters in copper irradiated near room temperature are predominantly vacancy type stacking fault tetrahedra. This implies that the interstitial-type defects, which according to MD simulations are predominantly in the form of small glissile interstitial clusters, do not efficiently interact with each other to form larger sessile defect clusters. Instead, many of the interstitials may escape to permanent sinks such as grain boundaries and dislocations. TEM investigations of copper irradiated over a wide range of doses [20,27,28,34] have found that the interstitial loop density reaches a maximum value at doses near 0.01 dpa. Irradiation at doses above ~0.01 dpa results in the creation of a low to moderate network dislocation density (~0.5 to $2 \times 10^{13}/m^2$), which is about an order of magnitude lower than that observed in other FCC neutron irradiated metals such as Ni or austenitic stainless steel [35].

In contrast to the defect cluster behavior observed in Cu, defect clusters visible by TEM are not produced in pure iron irradiated near room temperature to low doses of ~0.0001 dpa (Fig. 6). This may be attributed to the very low cascade production efficiency of defect clusters in irradiated iron [36,37], which in turn may be associated with the more open crystal lattice structure of BCC metals compared to the FCC structure. The defect cluster production efficiency increases with increasing atomic number for both FCC and BCC metals [36,37]. The defect clusters visible by TEM in Fe irradiated to doses of 0.01 dpa or higher (Fig. 6) were predominantly interstitial-type loops. It should be noted that a large number density of submicroscopic cavities (~$10^{24}/m^3$ for doses above 0.001 dpa) are also produced in iron irradiated near room temperature [34].

Figure 7 compares the temperature-dependent defect cluster densities of neutron irradiated Cu, Type 316 austenitic stainless steel, and V-4%Cr-4%Ti [38,39]. For each of these materials, there is a characteristic temperature above which the defect cluster density decreases rapidly. This so-called Stage V recovery temperature is associated with thermal instability of vacancy clusters (vacancy evaporation). In addition to directly contributing to a decrease in the visible density of vacancy-type defect clusters, the vacancies released from the clusters can also recombine with self-interstitial atoms in interstitial-type clusters and thereby contribute to their shrinkage and annihilation. The value of the Stage V temperature depends on damage rate (annealing time). In general there are a range of annealing activation energies, corresponding to the range of vacancy cluster sizes. In the case of Cu where the vacancy-type defect cluster size distribution is relatively narrow, an activation energy of ~0.84 eV for SFT annihilation has been obtained by data analysis [18]. Atomic-scale modeling of vacancy clusters in Cu has found similar results [40].
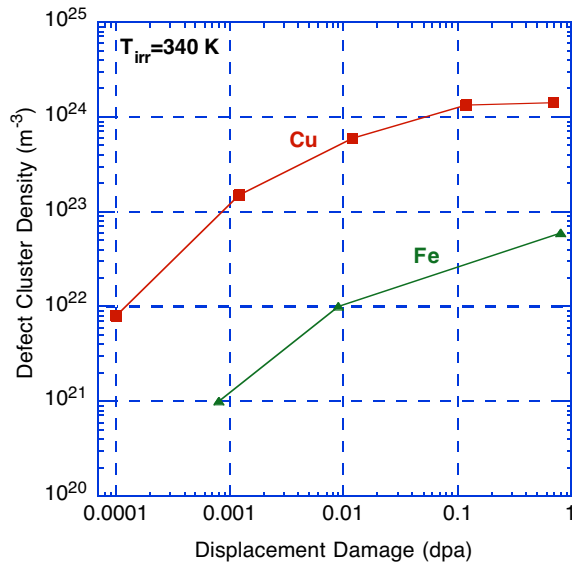
Figure 6. Comparison of the dose-dependent defect cluster accumulation of neutron irradiated Cu and iron [34].
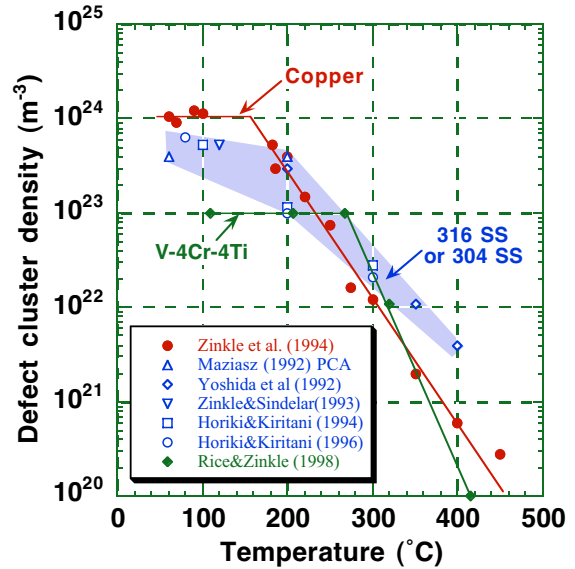
Figure 7. Summary of temperature dependence of defect cluster densities in neutron irradiated Cu, 316 austenitic stainless steel, and V-4%Cr-4%Ti [38,39].

DISLOCATION-DEFECT CLUSTER INTERACTIONS

The rapid defect cluster accumulation and concomitant pronounced hardening in metals irradiated at temperatures below electrical resistivity recovery stage V (~0.35 T_M) is responsible for significant loss of work hardening capacity in irradiated metals. This loss of work hardening capacity produces pronounced decreases in the uniform elongation, and was the topic of numerous studies performed in the 1960s. Although it was originally called "low temperature radiation embrittlement", a more appropriate term for the low uniform elongation observed following low-temperature irradiation is "loss of strain hardening capacity" (which may or may not be associated with a reduction in fracture toughness) [41]. A general feature associated with irradiation at low temperature (below ~0.3 T_M) is increased matrix hardness and decreased ductility due to the presence of radiation-induced defects which act as obstacles to dislocation motion, irrespective of alloy type or crystal structure. Based on systematic studies investigating surface slip lines and TEM microstructures in irradiated and deformed metals, the loss of ductility has been attributed to dislocation channeling [41-44]. Dislocation channeling occurs because the radiation-induced defect clusters present at these low temperatures can be readily cut by gliding dislocations (dislocation barrier strength of α~0.1-0.25, as opposed to 0.8 for impenetrable Orowan obstacles). This produces a defect-free path for subsequent dislocations emitted from the operating source.

Figure 8 shows an example of cleared dislocation channels produced in irradiated vanadium after room temperature deformation [45]. The irradiated microstructure consisted of a high density of small dislocation loops, and dislocation channeling was observed to occur on {110} and {112} lattice planes in the uniform gage region of the tensile specimen (0.3% uniform elongation). There was no evidence of deformation twins in the deformed vanadium [45]. Figure 9 shows cleared dislocation channels that formed in Type 316 austenitic stainless steel following irradiation to 0.78 dpa at 70°C and tensile deformation at room temperature [46]. Dislocation channeling was found to be the dominant deformation mode for stainless steel irradiated near room temperature to doses above 0.1 dpa. Dislocation arrays and twins occurred at lower doses. Dislocation channels have also been observed in irradiated ferritic/martensitic steel [47] and other engineering alloys [46] following deformation.
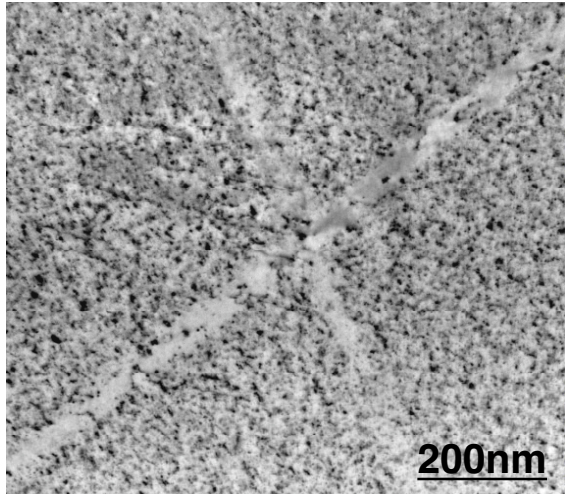
Figure 8. Cleared dislocation channels in pure vanadium irradiated to 0.012 dpa and tensile tested at room temperature [45].
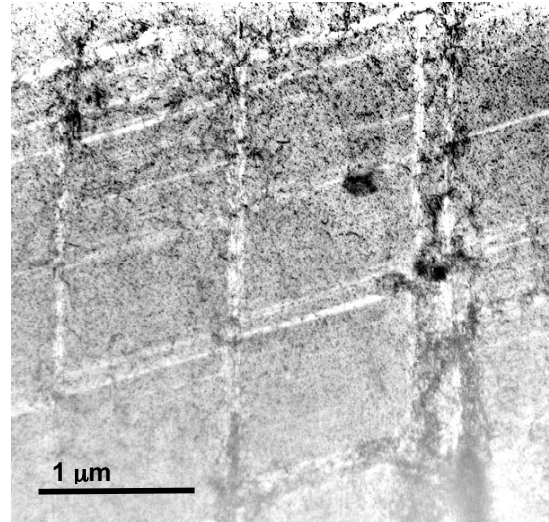

Figure 9. Cleared dislocation channels produced in Type 316 austenitic stainless steel (0.78 dpa, 32% elongation) [46].

The phenomenon of dislocation channeling has led to considerable interest regarding how SFTs and dislocation loops annihilate during plastic deformation, which is the fundamental process for creation of dislocation channels [45,46,48-51]. Figure 10 shows a series of photographs obtained from an in-situ TEM observation of dislocation-SFT interactions in a quenched gold specimen [51]. It is well established that the dislocation channeling phenomena in quenched gold is similar to what occurs in irradiated FCC metals [52,53]. In this series, the first moving dislocation interacted with the SFT at a position relatively close to the peak, compared with the second and the third dislocations. The second and the third dislocations moved along nearly the same glide plane, closer to the center of the SFT. Annihilation of the SFT occurred during interaction with the third dislocation, and a superjog was formed on the glide dislocation. The position of the small residual SFT corresponds to the top part of the two pieces cut by the first dislocation interaction with the original SFT. This indicates that only the base portion of the SFT is annihilated by dislocation interactions while the top portion survives. In addition, these in-situ dislocation-defect cluster interactions suggest that the location of the dislocation cutting reaction relative to the base of the SFT may be an important parameter. The in-situ TEM observations indicate that the cause of the SFT collapse is not associated with an unfaulting reaction triggered by the stress-field of the approaching dislocation, but instead is associated with direct interactions with the dislocation core. SFT annihilation following interaction with a single dislocation was also often observed in recent in-situ TEM deformation studies performed on quenched gold specimens [51].
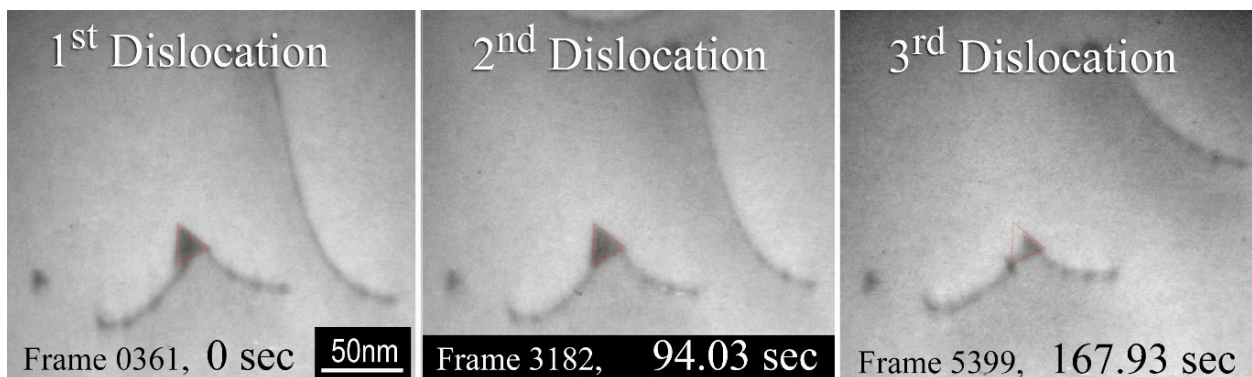

Figure 10. In-situ TEM still photo sequence of SFT annihilation by gliding dislocations [51].
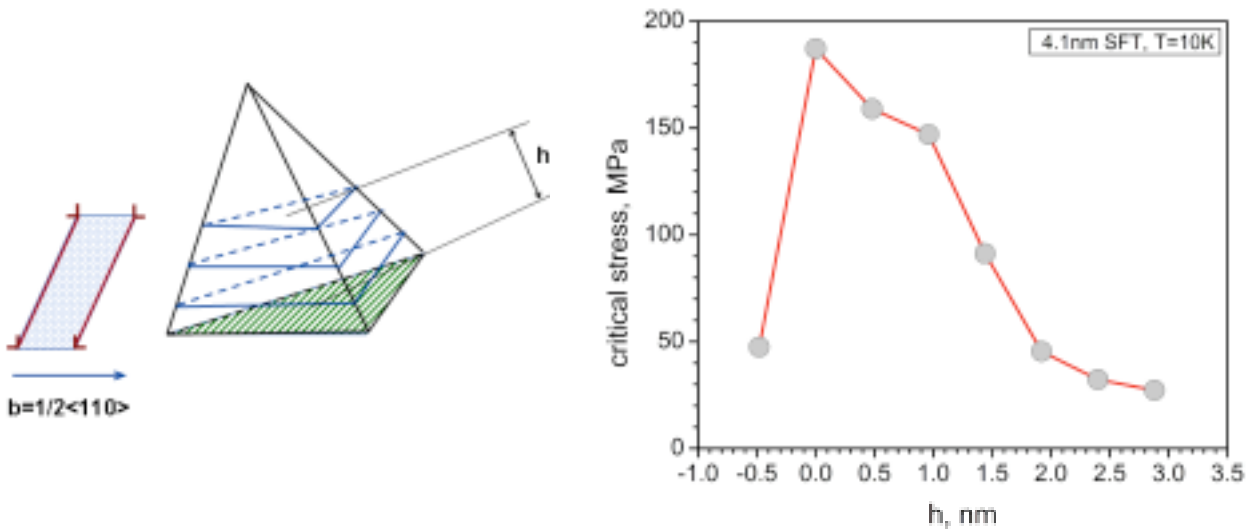
Figure 11. Effect of intersection height on the MD calculated critical shear stress for the interaction of a dislocation with regularly spaced SFTs in Cu at 10 K [54].

The barrier strength of SFTs has been recently examined by MD simulations for different glide plane positions relative to the SFT base [54]. Figure 11 shows schematically the geometry for dislocation interaction with an SFT. The glide dislocation with Burgers vector b=a/2<110> moves along a {111} glide plane and intersects the SFT at a distance h from the base of the SFT. The right hand graph in Fig. 11 summarizes the MD calculated critical dislocation barrier stress vs. distance from the SFT base for a 136 vacancy SFT (edge length L=4.2 nm) at 10 K. The SFT in the simulation were regularly spaced along the dislocation, with a separation distance of 35.5 nm. The simulation was performed at a strain rate of 2×10^6 s^{-1}, which corresponds to a dislocation velocity of 3 m/s. The critical stress is very high for dislocations intersecting the SFT near its base, and the stress decreases by nearly an order of magnitude for dislocations intersecting the SFT near its peak. An intermediate stress is observed for dislocations passing ~0.5 nm below the SFT base. Although the mechanism for SFT annihilation is still under investigation, these results suggest that application of stress above a threshold value may be an important factor for destruction of SFTs.

Based on the current state of knowledge obtained from in-situ and post-irradiation TEM deformation studies [43,51,55,56], it is apparent that SFTs and dislocation loops can be annihilated by interactions with gliding dislocations. Initial truncation of the SFT before the interaction with moving dislocations is not a crucial factor for the SFT collapse [51]. The interaction process appears to involve annihilation of the base portion of the SFT, whereas the upper portion of the SFT remains intact (corresponding to the two pieces separated during cutting by a moving dislocation). Successive interactions of the remnant SFT with glide dislocations may cause complete removal of the original SFT.

There are numerous details of dislocation interactions with defect clusters that remain to be understood. The reason why some SFTs can be collapsed by a single dislocation interaction, whereas the annihilation of other SFTs apparently require multiple dislocation interactions is unclear. There are also uncertainties regarding the detailed mechanism associated with the collapse of the base portion of the SFT, in particular whether the truncated base collapses to a loop prior to being absorbed by the incident gliding dislocation. In some cases, a superjog is formed on the interacting dislocation line whereas in other cases preliminary results indicate that a superjog is not formed. Furthermore, there remains a discrepancy between the fledgling MD simulation results and the in-situ TEM deformation studies regarding the possibility for collapse of perfectly formed SFTs. Recent MD simulations have found that dislocations cut perfectly formed SFTs but do not induce its collapse. SFT annihilation in MD simulations has so far been limited to energetically unstable overlapping truncated SFT configurations [48]. It is possible that the difference in effective

strain rates and dislocation velocity between the MD simulations ($\sim 10^6$ s^{-1}, 1-10 m/s) and experimental studies may be a contributing factor for this discrepancy. The effect of SFT size on interaction and annihilation processes also needs to be investigated. Finally, additional MD and experimental studies are needed to determine the detailed physical processes for loop-dislocation interactions.

Dislocation channeling is of practical importance because it can suppress normal dislocation network evolution processes, which are responsible for provide favorable work hardening characteristics that are essential for most structural material applications. Dislocation channeling begins to occur above a critical dose/hardening level (corresponding to N>$\sim 1\times 10^{23}$/m^3 for Cu tested at room temperature [18]). The physical cause of this process is still a topic of considerable debate (e.g., source vs. lattice hardening [57,58] discussions), and there is even debate in the literature whether dislocation channeling is the main factor responsible for the reduction of uniform elongation (versus lattice hardening effects) [46,59]. Determination of the physical mechanisms associated with dislocation interactions with radiation-induced defect clusters will be a key step in developing a more comprehensive understanding of the deformation behavior of irradiated metals and alloys.

CONCLUSIONS

Molecular dynamics simulations and transmission electron microscopy investigations are useful tools for investigating fundamental aspects of defect accumulation and defect cluster-dislocation interactions in irradiated materials. Continued advances in electron microscopy tools and computational simulations have recently enabled similar size scales to be examined via experiment and modeling with high spatial resolution (sub-nanometer detection capability). However, a large difference in accessible time scales for MD (~ 1 ns) and in-situ electron microscopy (>1 ms) still exists.

Many of the basic features of defect production in displacement cascades are now well established, including enhanced atomic mixing and point defect recombination during the cascade event, and the formation of subcascades at high energies. Quantitative differences in the behavior of pure FCC materials such as Cu and Ni are well established, although the detailed physical mechanism(s) responsible for their divergent behavior is not fully determined (melting temperature and electron-phonon coupling differences are considered to be important contributors). These differences in the initial defect production event (~ 1 ps time scale) can affect the subsequent microstructural evolution up to high damage levels (>1 dpa) and over long time scales of months or years, as evidenced by the difference in microstructural evolution behavior of Cu vs. Ni or stainless steel (i.e., dose-dependent morphology of defect clusters in Ni vs. SFT-dominant microstructure at all doses in Cu irradiated near room temperature). Numerous differences are apparent between pure BCC metals such as Fe and pure FCC metals, in particular regarding the formation of large planar vacancy clusters. Both FCC and BCC metals appear to have a strong tendency to form small glissile interstitial clusters. The practical role of small glissile interstitial clusters in the long-term microstructural evolution of high purity metals and engineering alloys needs further research.

Dislocation channeling is a common but not universal deformation mode for irradiated materials. It becomes prevalent in metals and alloys irradiated above 0.01 to 0.1 dpa at temperatures below ~ 0.3 T$_M$, where T$_M$ is the melting temperature. Pronounced decreases in uniform elongation are observed when dislocation channeling becomes the dominant deformation mechanism. Since annihilation of radiation-induced defect clusters is a key step in the formation of cleared dislocation channels, recent research has focused on the interactions between defect clusters and gliding dislocations. In-situ TEM deformation studies have demonstrated the direct annihilation of individual defect clusters by gliding dislocations. The effects of strain rate, test temperature, defect cluster size and morphology need further investigation.

Acknowledgements

REFERENCES

1. S.J. Zinkle and B.N. Singh, J. Nucl. Mater. **199**, 173 (1993).
2. M.J. Norgett, M.T. Robinson, and I.M. Torrens, Nucl. Eng. Des. **33**, 50 (1975).
3. R.S. Averback, R. Benedek, and K.L. Merkle, Phys. Rev. B **18** (8), 4156 (1978).
4. R.S. Averback, J. Nucl. Mater. **216**, 49 (1994).
5. R. E. Stoller and L.E. Greenwood, in *20th Int. Symp. on Effects of Radiation on Materials*, ASTM STP 1405, edited by S.T. Rosinski, M.L. Grossbeck, T.R. Allen, and A.S. Kumar (American Society for Testing and Materials, West Conshohocken, PA, 2001), p. 204.
6. Yu.N. Osetsky, D.J. Bacon, and B.N. Singh, J. Nucl. Mater. **307-311**, 866 (2002).
7. D.J. Bacon, F. Gao, and Yu.N. Osetsky, J. Nucl. Mater. **276**, 1 (2000).
8. R.E. Stoller, J. Nucl. Mater. **276**, 22 (2000).
9. R.E. Stoller, J. Nucl. Mater. **283-287**, 746 (2000).
10. Yu.N. Osetsky and D.J. Bacon, Nucl. Instr. Meth. B **180**, 85 (2001).
11. R.E. Stoller, G.R. Odette, and B.D. Wirth, J. Nucl. Mater. **251**, 49 (1997).
12. D.J. Bacon, A.F. Calder, F. Gao, V.G. Kapinos, and S.J. Wooding, Nucl. Instr. Meth. B **102**, 37 (1995).
13. W.J. Phythian, R.E. Stoller, A.J.E. Foreman, A.F. Calder, and D.J. Bacon, J. Nucl. Mater. **223**, 245 (1995).
14. B.D. Wirth, G.R. Odette, D. Maroudas, and G.E. Lucas, J. Nucl. Mater. **276**, 33 (2000).
15. K. Nordlund and F. Gao, Appl. Phys. Lett. **74** (18), 2720 (1999).
16. B.D. Wirth, V. Bulatov, and T. Diaz de la Rubia, J. Nucl. Mater. **283-287**, 773 (2000).
17. D.J. Bacon, Yu.N. Osetsky, R.E. Stoller, and R.E. Voskoboinikov, J. Nucl. Mater. **323**, 152 (2003).
18. S.J. Zinkle, Radiat. Eff. Def. Solids **148**, 447 (1999).
19. Yu.N. Osetsky, D.J. Bacon, A. Serra, B.N. Singh, and S.I. Golubov, J. Nucl. Mater. **276**, 65 (2000).
20. S.J. Zinkle and L.L. Snead, J. Nucl. Mater. **225**, 132 (1995).
21. J. Diehl and W. Schilling, in *3rd Intern. Conf. on Peaceful Uses of Atomic Energy*, (United Nations, New York, 1965), Vol. 9, p. 72.
22. T. Diaz de la Rubia, R.S. Averback, H. Hsieh, and R. Benedek, J. Mater. Res. **4** (3), 579 (1989).
23. M.L. Jenkins, M.A. Kirk, and W.J. Phythian, J. Nucl. Mater. **205**, 16 (1993).
24. I.M. Robertson, D.K. Tappin, and M.A. Kirk, Philos. Mag. A **68** (5), 843 (1993).
25. S.J. Zinkle, J. Nucl. Mater. **150**, 140 (1987).
26. S.J. Zinkle and K. Farrell, J. Nucl. Mater. **168**, 262 (1989).
27. S.J. Zinkle and B.N. Singh, J. Nucl. Mater. **283-287**, 306 (2000).
28. S.J. Zinkle, A. Horsewell, B.N. Singh, and W.F. Sommer, J. Nucl. Mater. **212-215**, 132 (1994).
29. M. Kiritani, J. Nucl. Mater. **155-157**, 113 (1988).
30. Y. Dai, "Mechanical properties and microstructures of copper, gold and palladium single crystals irradiated with 600 MeV protons," Ph.D. Thesis, Lausanne, EPFL, 1995.
31. S.J. Zinkle and G.L. Kulcinski, J. Nucl. Mater. **122&123**, 449 (1984).
32. S.J. Zinkle, in *15th Int. Symp. on Effects of Radiation on Materials*, ASTM STP 1125, edited by R.E. Stoller, A.S. Kumar, and D.S. Gelles (American Society for Testing and Materials, Philadelphia, 1992), p. 813.
33. T. Muroga, H.L. Heinisch, W.F. Sommer, and P.D. Ferguson, J. Nucl. Mater. **191-194**, 1150 (1992).
34. M. Eldrup, B.N. Singh, S.J. Zinkle, T.S. Byun, and K. Farrell, J. Nucl. Mater. **307-311**, 912 (2002).

35. S.J. Zinkle, P.J. Maziasz, and R.E. Stoller, J. Nucl. Mater. **206**, 266 (1993).
36. M.A. Kirk, I.M. Robertson, M.L. Jenkins et al., J. Nucl. Mater. **149**, 21 (1987).
37. C.A. English and M.L. Jenkins, Mater. Sci. Forum **15-18**, 1003 (1987).
38. P.M. Rice and S.J. Zinkle, J. Nucl. Mater. **258-263**, 1414 (1998).
39. A.F. Rowcliffe, S.J. Zinkle, J.F Stubbins, D.J. Edwards, and D.J. Alexander, J. Nucl. Mater. **258-263**, 183 (1998).
40. Yu.N. Osetsky, A. Serra, M. Victoria, S.I. Golubov, and V. Priego, Philos. Mag. A **79**, 2285 (1999).
41. S.J. Zinkle and G.E. Lucas, in *Fusion Materials Semiannual Progress Report for Period ending June 30, 2003, DOE/ER-0313/34*, (Oak Ridge National Lab, 2003), p. 101.
42. J.V. Sharp, Radiat. Eff. **14**, 71 (1972).
43. M.S. Wechsler, in *The Inhomogeneity of Plastic Deformation*, edited by R.E. Reed-Hill (Am. Society for Metals, Metals Park, OH, 1972), p. 19.
44. A. Luft, Prog. Mater. Sci. **35**, 97 (1991).
45. N. Hashimoto, T.S. Byun, K. Farrell, and S.J. Zinkle, J. Nucl. Mater., Proc. 11th Int. Conf. on Fusion Reactor Materials, Kyoto, Dec. 7-11, 2003, in press (2004).
46. K. Farrell, T.S. Byun, and N. Hashimoto, Report No. ORNL/TM-2002/63, 2003.
47. N. Hashimoto, M. Ando, H. Tanigawa et al., Fusion Science and Technology **44** (2), 490 (2003).
48. B.D. Wirth, V. Bulatov, and T. Diaz de la Rubia, J. Eng. Mater. and Technol. **124**, 329 (2002).
49. N. Hashimoto, S.J. Zinkle, A.F. Rowcliffe, J.P. Robertson, and S. Jitsukawa, J. Nucl. Mater. **283-287**, 528 (2000).
50. N. Hashimoto, S.J. Zinkle, R.L. Klueh, A.F. Rowcliffe, and K. Shiba, in *Microstructural Processes During Irradiation-2000*, MRS Symposium Proceedings, edited by R.G. Elliman (Materials Research Society, Warrendale, PA, 2001), Vol. 650, p. R1.10.1.
51. Y. Matsukawa and S.J. Zinkle, J. Nucl. Mater., Proc. 11th Int. Conf. on Fusion Reactor Materials, Kyoto, Dec. 7-11, 2003, in press (2004).
52. S. Yoshida, M. Kiritani, Y. Deguchi, and N. Kamigaki, Trans. JIM **9** Supplement (Proc. ICSMA-1), 83 (1968).
53. M.S. Bapna and M. Meshii, Mater. Sci. Eng. **16**, 181 (1974).
54. Yu.N. Osetsky, R.E. Stoller, and Y. Matsukawa, J. Nucl. Mater., Proc. 11th Int. Conf. on Fusion Reactor Materials, Kyoto, Dec. 7-11, 2003, in press (2004).
55. E. Johnson and P.B. Hirsch, Philos. Mag. A **43** (1), 157 (1981).
56. K. Noda, H. Saka, K. Shiraishi, H. Yoshida, and T. Imura, in *Proc. 5th Intern. Conf. on High Voltage Electron Microscopy, Kyoto*, (Japanese Soc. of Electron Microscopy, Tokyo, 1977), p. 403.
57. M.J. Makin and J.V. Sharp, Phys. Stat. Sol. **9**, 109 (1965).
58. B.N. Singh, A.J.E. Foreman, and H. Trinkaus, J. Nucl. Mater. **249**, 103 (1997).
59. G.R. Odette, M.Y. He, E.G. Donahue, P. Spätig, and T. Yamamoto, J. Nucl. Mater. **307-311**, 171 (2002).